

Numerical simulation of type II primordial black hole formation

Koichiro Uehara,^a Albert Escrivà,^a Tomohiro Harada,^b
Daiki Saito,^a and Chul-Moon Yoo^a

^aDivision of Science, Graduate School of Science, Nagoya University, Nagoya 464-8602, Japan

^bDepartment of Physics, Rikkyo University, Toshima, Tokyo 171-8501, Japan

E-mail: uehara.koichiro.p8@s.mail.nagoya-u.ac.jp,
escriva.manas.albert.y0@a.mail.nagoya-u.ac.jp, harada@rikkyo.ac.jp,
saito.daiki.g3@s.mail.nagoya-u.ac.jp, yoo.chulmoon.k6@f.mail.nagoya-u.ac.jp

Abstract. This study investigates the formation of type II primordial black holes (PBHs) resulting from extremely large amplitudes of initial fluctuations in a radiation-dominated universe. We find that, for a sufficiently large initial amplitude, the configuration of trapping horizons shows characteristic structure due to the existence of bifurcating trapping horizons. We call this type of configuration of the trapping horizons type II-B PBH, while the structure without a bifurcating trapping horizon type II-A PBH. In Ref. [1], in the dust-dominated universe, the type B PBH can be realized by the type II initial fluctuation, which is characterized by a non-monotonic areal radius as a function of the radial coordinate (throat structure) in contrast with the standard case, type A PBH with a monotonic areal radius (type I fluctuation). Our research reveals that a type II fluctuation does not necessarily result in a type B PBH in the radiation-dominated case. We also find that for an initial amplitude well above the threshold value, the resulting PBH mass may either increase or decrease with the initial amplitude, depending on its specific profile rather than its fluctuation type.

ArXiv ePrint: [2401.06329](https://arxiv.org/abs/2401.06329)

Contents

1	Introduction	1
2	Initial data setting	3
3	Spacetime structure and definition of type A/B PBHs	6
3.1	Time evolution of type I/II fluctuations	6
3.2	Identification of BH apparent horizon	6
3.3	Spacetime structures of type A/B PBH	8
4	PBH mass	11
4.1	PBH mass with the Gaussian initial fluctuation	11
4.2	PBH mass with the initial fluctuation motivated by the three-zone model	14
5	Conclusion	15
A	Conformal diagrams of the three-zone model for the dust case	17
B	Derivation of ζ_{cFLRW} in radial coordinate r	18
C	Double-peaked compaction function and averaged density perturbation in the type II fluctuation	21

1 Introduction

Primordial black holes (PBHs) play a crucial role in exploring the early universe, particularly in investigating inhomogeneities whose scales are much smaller than those of the fluctuations probed by the cosmological microwave background. Since PBHs are remnants of nonlinear inhomogeneity in the primordial universe following the inflationary era, they are unique probes of statistical properties of the small-scale primordial inhomogeneity. They are considered as one of the candidates for dark matter and can be detected as black hole (BH) binaries by gravitational wave interferometers. According to the standard scenario, PBHs were formed through the gravitational collapse of significantly high-density regions during the radiation-dominated era, which had been generated in the inflationary period [2–6].

The mechanism of PBH formation can be briefly understood by considering a model of the gravitational collapse in the flat Friedmann–Lemaître–Robertson–Walker (FLRW) universe (see, e.g., Refs. [7, 8]). A criterion for the collapse has been first proposed by Carr [9] as $\delta \gtrsim w = 1/3$, where δ is the amplitude of the density perturbation, and w is the coefficient of the assumed linear equation of state $p = w\rho$ with p and ρ being the pressure and the energy density, respectively. A more accurate threshold value has been explored by numerically analyzing general relativistic nonlinear dynamics [7, 10–23].

In cosmological perturbation theory, the growth of the perturbation is often described by the evolution of the curvature perturbation ζ , which represents the growing adiabatic modes. To perform numerical simulations of PBH formation, one must establish the initial conditions for the spacetime geometry and the fluid in the system. This involves setting the initial profile of curvature fluctuations at the super-horizon scale before the horizon entry

to be consistent with the assumption of the growing adiabatic modes. These analytical constructions are typically achieved using the gradient expansion techniques [11, 16, 21].

In a spherically symmetric system, we introduce a type II primordial fluctuation characterized by a non-monotonic behavior of the areal radius $R = \sqrt{A/4\pi}$, where A is the area of the 2-sphere as a function of the radial coordinate r with constant t . These fluctuations exhibit distinct neck-like structures, with a minimal areal radius at $\partial_r R = 0$. In cosmological perturbation theory, the areal radius R is often expressed via the curvature fluctuation ζ , $R \propto re^\zeta$. The type II fluctuation is only realized by a sufficiently large amplitude of ζ with the scale fixed.

Kopp, Hofmann, and Weller (KHW) [1] investigated PBH formation associated with the type II fluctuations by employing the Lemaître–Tolman–Bondi (LTB) solution, which is the analytic solution for the dust fluid ($w = 0$). They investigated the causal structure of the spacetime generated from a specific profile of the type II fluctuation. They explicitly showed that it describes a spacetime of BH formation, which they call type II PBH. In addition, they revealed distinct properties of the type II PBH from the type I PBH, which arises from typical type I fluctuations with the amplitude above the threshold. Carr and Harada [24] analytically discussed type II PBHs with more general equations of state using simplified models. Type I/II fluctuations are also important because the threshold of these two cases gives a possible maximum value of the averaged density perturbation at horizon entry in the simplified models [1, 24]. We aim to investigate the dynamics and the spacetime structure of type II PBH formation in the radiation-dominated universe, namely, to clarify the impact of the existence of the radiation pressure.

When we consider the abundance of PBHs, the contribution from type II fluctuations is often neglected because they are highly unlikely to be generated statistically, and the abundance of type II PBHs originating from them is typically suppressed. However, as mentioned in [25], they can be significant when the statistics of primordial fluctuations are highly non-Gaussian. Moreover, in the context of a single-field inflationary model, it has been recently discovered in Ref. [26] that type II fluctuations surround the bubbles formed when the inflaton overshoots the barrier. As non-Gaussianities increase, the production of vacuum bubbles becomes dominant, leading to a mass function and abundance primarily driven by these fluctuations. In addition, a similar BH formation mechanism due to the birth of a baby universe with a tunneling process during inflation has been reported in Refs. [27, 28]. The baby universe is connected to our universe through a throat inside the BH, like the neck structure in the type II fluctuation.

If one would like to follow the time evolution of the type II fluctuations via a usual areal radial coordinate system such as in Ref. [21], the neck throat structure would be complicated. In the Misner–Sharp formalism [29] (see also Refs. [1, 30]), the evolution equations suffer from the trouble associated with 0/0 term at the neck radius satisfying $\partial_r R = 0$ when we consider type II fluctuations. To overcome this problem, it is necessary to conveniently use and modify the equations, as done in Ref. [27] for another scenario of PBH formation from the collapse of vacuum bubbles.

On the other hand, in this paper, we use the simulation code developed from a 3+1 dimensional simulation code [31] with BSSN [32, 33] formalism with CARTOON method [34], so that we can avoid the same problem.

This paper is organized as follows. Section 2 describes the setup and numerical code of spherically symmetric numerical simulation of PBH formation. In Section 3.1, we present the simulation results, highlighting the time evolution of fluctuations. Then, we explore

the formation of trapping horizons, including the BH horizon in Section 3.2, and give an interpretation of the resulting trapping horizon configurations in Section 3.3. In Section 4, we examine the evolution of PBH mass. In Section 4.2, to check the profile dependence of the PBH mass, we explore PBH formation from another initial profile that models the overdense region, as described by KHW. Finally, we offer our conclusions in the last section. Appendix A provides the conformal diagrams of the exact three-zone solutions for PBH formation. Appendix B provides the derivation of the curvature perturbation for the three-zone model. Appendix C proves the appearance of two peaks in the compaction function and the averaged density perturbation for the type II fluctuation.

Throughout the paper, we use the geometrical unit in which the speed of light and the gravitational Newton constant are unity, that is, $c = G = 1$.

2 Initial data setting

We start our simulation from the time when the length scale of the fluctuation is much larger than the Hubble length H_b^{-1} , that is, $k^{-1} \gg (aH_b)^{-1}$ with k , $a = a(t)$ and $H_b := (da/dt)/a$ being the characteristic comoving wave number, the scale factor and the Hubble parameter of the background flat FLRW universe, respectively. We obtain the initial condition by applying the cosmological long-wavelength approximation, in which the small parameter $\epsilon := k/(aH_b)$ is introduced¹, and the zeroth order spatial metric is given by [35]

$$\gamma_{ij} = a^2(t)e^{2\zeta(x^k)} f_{ij}, \quad (2.1)$$

with f_{ij} being the reference 3-metric of the background flat geometry, and $\partial_i \zeta / (aH_b) = \mathcal{O}(\epsilon)$. We note that the function ζ is a time-independent arbitrary function of the spatial coordinates x^k . Once we initially set ζ as a function of the spatial coordinates x^i and fix the gauge conditions, we can successively obtain the growing mode solution up to the following leading terms in this expansion [11, 21]. These long-wavelength solutions are used as the initial data for the time evolution. In this paper, we initially fix the gauge by imposing the constant mean curvature slice (uniform Hubble slice) and the normal threading, for which the trace of the extrinsic curvature of the time slice is uniformly given by $-3H_b$ and the shift vector is equal to zero.

In a spherically symmetric system, the line element at the zeroth order in powers of ϵ is denoted as

$$ds^2 = -dt^2 + a^2(t)e^{2\zeta(r)}(dr^2 + r^2 d\Omega^2), \quad (2.2)$$

where $d\Omega^2$ represents the line element of a 2-sphere. We can see that the areal radius is given by $R = ar e^\zeta$ in this line element. Throughout this paper, to resolve the fine structure, such as the trapping horizon formation near the center $r = 0$, we use the scale-up coordinate z , which is defined as

$$r = z - \frac{\eta}{1 + \eta} \frac{L}{\pi} \sin\left(\frac{\pi}{L} z\right) \quad (2.3)$$

with a parameter $\eta = 20$ [31]. In this coordinate, the resolution in the central region is $1 + 2\eta$ times finer than that around the boundary $z = r = L$;

$$\left. \frac{dr}{dz} \right|_{r=L} = (1 + 2\eta) \left. \frac{dr}{dz} \right|_{r=0}. \quad (2.4)$$

¹One would use the other expression, $\epsilon := 1/(H_b R_m)$ with $R_m \propto a/k$ being the areal radius, where $\mathcal{C}_{SS}(r)$ takes a maximum.

Up through section 4, we use the following Gaussian-shaped profile in the numerical simulation [31],

$$\zeta(r) = \mu e^{-\frac{1}{2}k^2 r^2} W(r), \quad (2.5)$$

where μ is the amplitude of the fluctuation and $W(r)$ is a window function [31] introduced to eliminate the tail of the Gaussian function and impose $\zeta = 0$ at the outer boundary of the numerical domain.²

Figure 1 shows the functional form of this profile (left) and the areal radius R (right). By taking a sufficiently large amplitude of the fluctuation μ , the areal radius $R(r)$ of the perturbed region becomes non-monotonic along the radial coordinate r , i.e., a pair of the local minimum and maximum points appears with $\partial_r R = 0$ for $\mu \gtrsim 1.4$ as in Fig. 1. We call this structure the neck or throat structure, and KHW defined such fluctuations as type II and distinguished them from type I fluctuations, which have a monotonic areal radius [1].

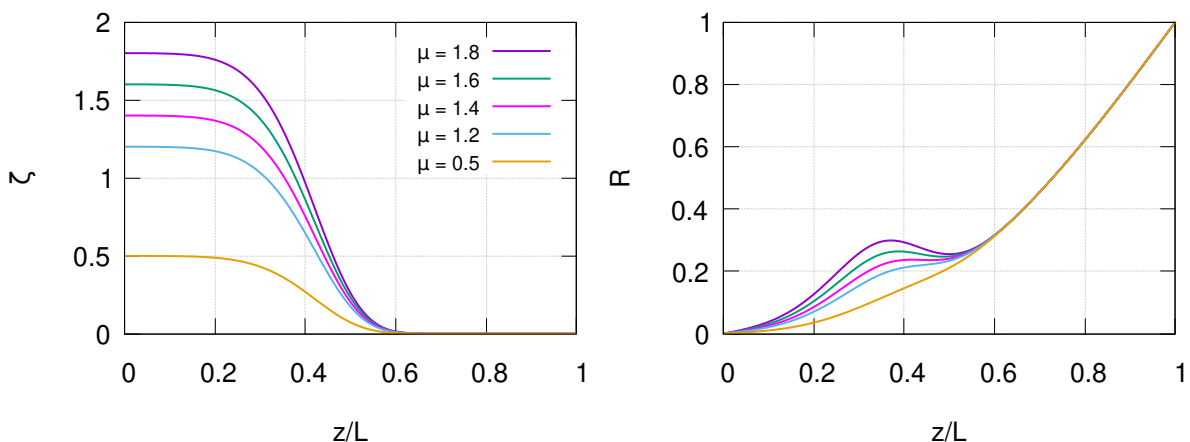


Figure 1. Initial profile of the curvature fluctuation ζ (left) and areal radius R as functions of the scale-up coordinate radius z/L . By taking the amplitude parameter μ larger, a type II fluctuation appears for $\mu = 1.4$ and above with the neck $\partial_r R = 0$.

The feature of type II fluctuations can also be understood as two peaks³ of the Shibata–Sasaki compaction function \mathcal{C}_{SS} defined by

$$\mathcal{C}_{SS}(r) = \frac{1}{2} \left[1 - \left(1 + r \frac{d\zeta}{dr} \right)^2 \right] = \frac{1}{2} \left[1 - \left(\frac{r}{R} \frac{dR}{dr} \right)^2 \right]. \quad (2.7)$$

This function has been firstly introduced in Ref. [11] as an estimator for the criterion of PBH formation, and its usefulness has been recognized through subsequent related works (see

²The explicit functional form [31] is

$$W(r) = \begin{cases} 1 & \text{for } 0 \leq r \leq r_w, \\ 1 - \frac{((r_w - L)^6 - (L - r)^6)^6}{(r_w - L)^{36}} & \text{for } r_w \leq r \leq L, \\ 0 & \text{for } L \leq r, \end{cases} \quad (2.6)$$

where r_w is set to $0.8L$.

³It is shown in Ref. [26] that the appearance of fluctuations of type II naturally appears via a specific single-field inflation model with a bump, but in this case, one of the peaks of \mathcal{C}_{SS} is hidden inside the bubble.

Ref. [36] and references therein for details including its relations to legitimate compaction functions in different gauges and physical interpretations). The outer peak of \mathcal{C}_{SS} corresponds to the neck in the type II fluctuation, the radius at which the areal radius takes the minimum value considered relevant for PBH formation. We will give a general proof for two peaks and the minimum between them for the compaction function in the type II fluctuation in the Appendix C. We focus on the two peak configurations associated with type II fluctuations (see also Ref. [37] for two peak configurations with fluctuations of type I). The form of the compaction function for the specific function of ζ (2.5) is shown in Fig. 2. By using the position of the peak of $\mathcal{C}_{\text{SS}}(r)$, $r_m = \sqrt{2}/k$, we analytically obtain the threshold value $\mu_{c,\text{II}} = e/2 = 1.359\dots$ for fluctuations of type II.⁴ For $\mu > \mu_{c,\text{II}}$ the compaction function takes the maximum value of 0.5 at least one location with the radial coordinate, and the number of peak positions becomes two, r_{m1} and r_{m2} with $r_{m1} < r_{m2}$. This implies that type II fluctuations always reach the collapse threshold and form PBHs irrespectively of the initial $\zeta(r)$ profile. The isotropic coordinate r does not always give the geometrical size of the enclosed region, which can often lead to misunderstanding. Therefore, we also explicitly show the compaction function \mathcal{C}_{SS} as a function of the areal radius R in the right panel of Fig. 2, which will be contrasted with the right panel of Fig. 13.

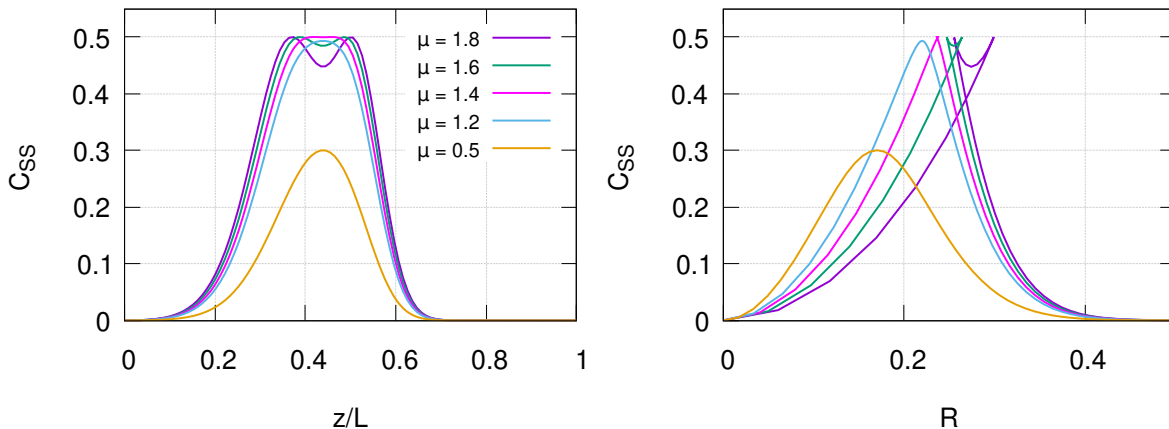


Figure 2. Compaction function \mathcal{C}_{SS} . The horizontal axes are the scale-up coordinate radius z/L (left) and the areal radius R (right). By taking the amplitude μ larger, the number of peaks becomes two for $\mu \simeq 1.4$ and above, corresponding to type II fluctuations.

To follow the time evolution of gravitational collapse from the initial profile of fluctuation, we use the numerical code COSMOS-S [38–40] based on a 3+1 dimensional code of fourth order Runge–Kutta method with BSSN formalism [32, 33]. This code is specialized for spherically symmetric systems using the CARTOON method [34]. We consider the time evolution of the initial fluctuation given by the functional form of ζ (2.5) with the equation of state parameter $w = 1/3$, namely, radiation fluid. Here, the asymptotically spatially flat FLRW boundary condition is implemented as in Ref. [11]. However, we could not avoid violating the constraint at the outer boundary, which propagates into the bulk region. Therefore, in the following analyses, we terminate the time evolution before the violation reaches the central region relevant for the analyses of PBH formation.

⁴Here, we ignore the window function $W(r)$ to estimate the location $r_m = \sqrt{2}/k$ of the peak of compaction function $\mathcal{C}_{\text{SS}}(r)$ since this acts on $\zeta(r)$ only near the outer boundary, $r = r_w = 0.8L$.

We also find the constraint violation near the center for cases where an apparent horizon forms. Nevertheless, since we find both independent future-directed null directions inward, the constraint violation does not propagate outward. In practice, we excise several grids inside the apparent horizon to avoid a numerical calculation crash if needed.

We take the coordinate size L of the numerical region ($0 \leq z \leq L$ or equivalently $0 \leq r \leq L$) as the unit length scale and set the initial value of the scale factor to unity. We fix the ratio between the initial Hubble background length H_b^{-1} and the typical scale k^{-1} of the initial fluctuation as $k^{-1} = 10H_b^{-1}$ that ensures the long-wavelength approximation. To avoid propagating the constraint violation, we need to take a larger region than the initial Hubble length for a longer duration of the time evolution. In the following, we take $H_b^{-1} = 0.01L$ or $H_b^{-1} = 0.005L$ depending on the duration of the required time evolution. The horizon entry time t_H is defined as $k^{-1} = (aH_b)^{-1}|_{t=t_H}$ throughout this paper.

3 Spacetime structure and definition of type A/B PBHs

3.1 Time evolution of type I/II fluctuations

First, we show the time evolutions of the fluid energy density and the lapse function in Fig. 3 for $\mu = 0.5, 1.2$, and 1.8 . For the cases of type I fluctuations $\mu = 0.5$ (left) and $\mu = 1.2$ (middle), the former disperses, but the latter contracts and forms a peak at the center in the density plot in Fig. 3. The latter case (middle) indicates a typical gravitational collapse, for which the lapse is decreasing to a very small value as plotted in Fig. 3 as in Ref. [40]. For a type II fluctuation case $\mu = 1.8$ (right), the collapsing behavior occurs similarly to the $\mu = 1.2$ (middle) case in the density and lapse plots.

To check the convergence of the simulation, we plot the spatial average value of the Hamiltonian constraint⁵ [21](Fig. 4). One can find roughly quadratic convergence in the different spatial resolutions, and it is consistent with our numerical code with a second-order scheme implemented in evaluating the fluid flux.

3.2 Identification of BH apparent horizon

First, we introduce two independent future-directed radial null vector fields, l and l' . We also define the null expansion for l and l' as θ and θ' . A null expansion is expressed as $\theta := 2\mathcal{L}_l R/R$, where \mathcal{L}_l denotes the Lie derivative along l . Trapping horizons are defined by the surfaces that satisfy $\theta\theta' = 0$ or equivalently the compactness $2M/R = 1$ with M being the Misner–Sharp mass defined by $M(t, r) := R(1 - \nabla_\mu R \nabla^\mu R)/2$ [8, 29, 41, 42].

In Fig. 5, the snapshots of the compactness $(2M/R)(z)$ are plotted. For $\mu = 0.5$, the intersection between $(2M/R)(r)$ and the horizontal line of $2M/R = 1$ is always only one. On the other hand, for the cases $\mu = 1.2$ and 1.8 , the line intersects $2M/R = 1$ more than three times at a sufficiently late time. The worldlines of the intersections are shown in Fig. 6. To identify future-trapped ($\theta < 0$ and $\theta' < 0$) and past-trapped ($\theta > 0$ and $\theta' > 0$) regions, we also show directions of two independent null vector fields l and l' together with the contour curves of the areal radius in Figs. 7 and 8. Comparing the directions of the null vector fields and the contour curves of the areal radius, we can realize that the red and blue shaded regions in Fig. 6 are future- and past-trapped regions, respectively. More specifically, in the future(past)-trapped region, both arrows direct to directions along which

⁵First, we evaluate the appropriately normalized value of the constraint violation \mathcal{H}_p at each grid point labeled by p . Then the average is taken as $\sum_{p=1}^N \mathcal{H}_p/N$, where N is the total number of the grid.

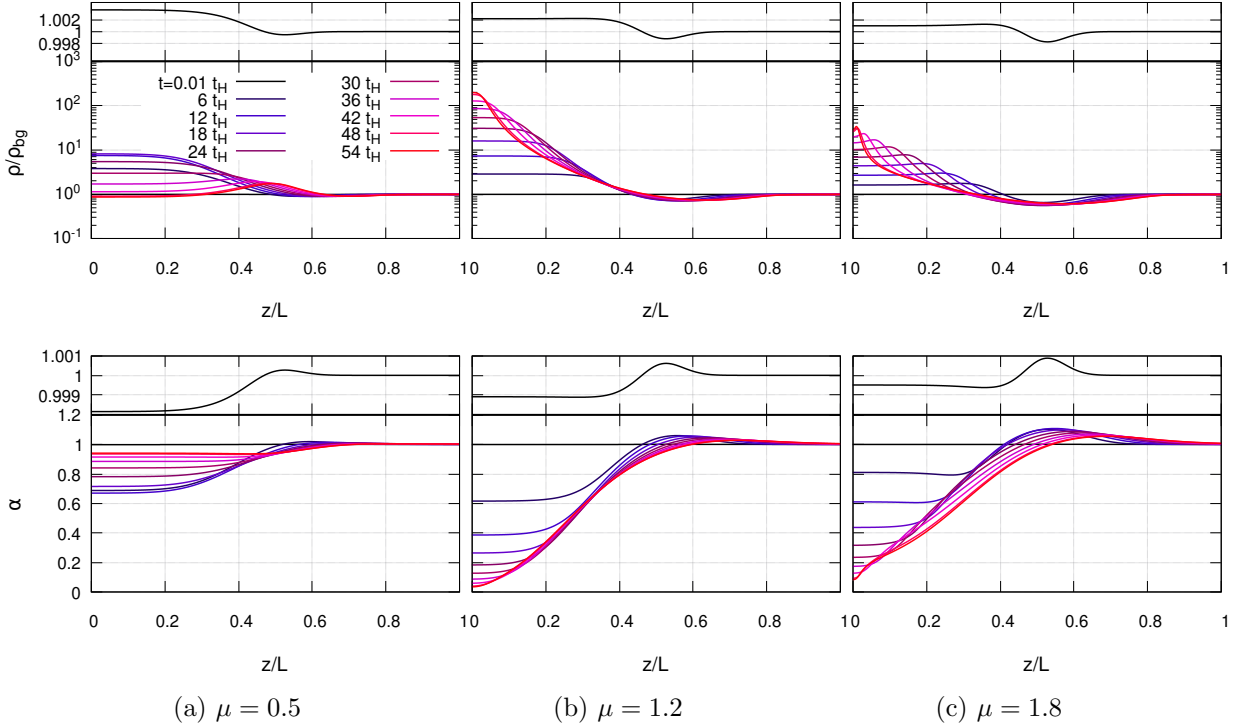


Figure 3. Snapshots of the fluid energy density contrast ρ/ρ_{bg} and lapse function α of type I fluctuations (left and middle) and a type II fluctuation (right). The initial configurations ($t = 0.01 t_H$) are shown in black on a different scale.

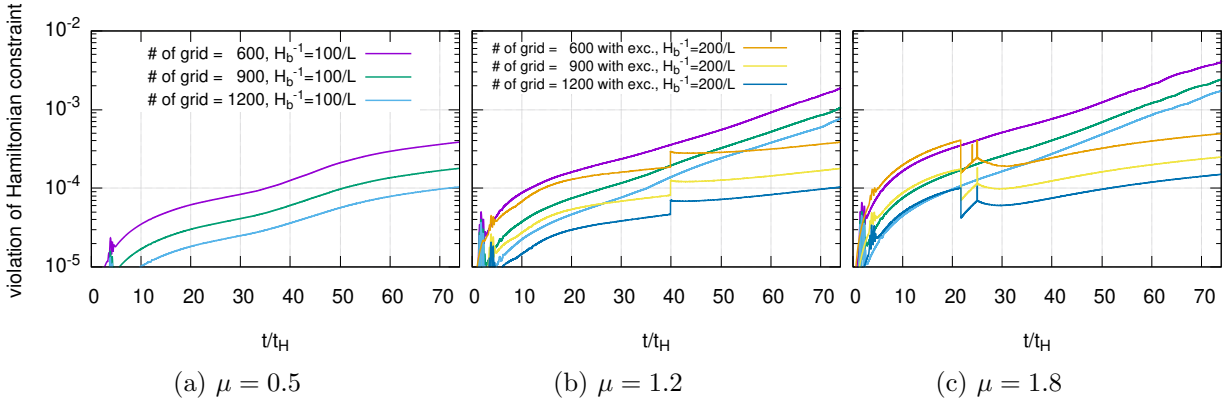


Figure 4. The average value of the Hamiltonian constraint violation with different resolutions of the number of grid points for three typical cases for no collapse (left), collapse from a type I fluctuation (middle), and collapse from a type II fluctuation (right), respectively. The horizontal axis is a time coordinate normalized by the time of the horizon entry. We use the simulation result to $t = 50 t_H$ to evaluate spacetime structures around horizon formation before the violation propagation reaches the bulk region from the outer boundary. For evaluating a longer time evolution of the PBH mass, the average is taken outside the BH apparent horizon (or the future-outer trapping horizon, described in Sec. 3.2) after the horizon formation at around $t = 40 t_H$ for $\mu = 1.2$ and $t = 24 t_H$ for $\mu = 1.8$.

the areal radius decreases (increases), and the curve described by red points indicates the

boundary satisfying $\theta\theta' = 0$. Then, we refer to a marginally future-trapped surface that is the outer boundary of the future-trapped region on the $t = \text{const}$ hypersurface as a BH apparent horizon. Similarly, we refer to a marginally past-trapped surface that is the inner boundary of the past-trapped region on the $t = \text{const}$ hypersurface as a cosmological apparent horizon.

It is not easy to understand the horizon configuration. Therefore, we carefully investigate it and present a more concrete classification of trapping horizons in the following sections. Readers who would like to get a quick intuition about the horizon configuration can refer to the schematic conformal diagram in Figures 16 and 17.

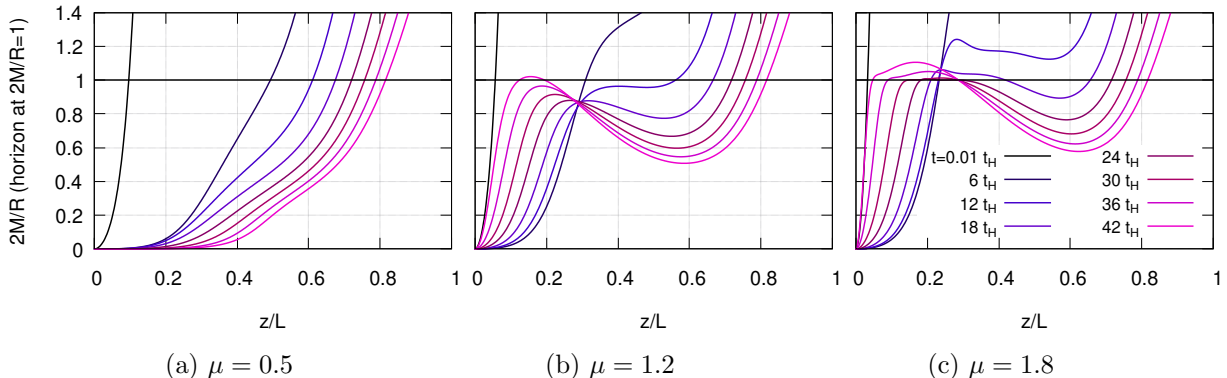


Figure 5. Snapshots of the compactness $2M(t, r)/R(t, r)$. For the $\mu = 1.2$ case, the trapping horizon at the center is formed at around $t = 40t_H$ (middle). For the $\mu = 1.8$ case, the horizon is formed at around $t = 24t_H$ (right).

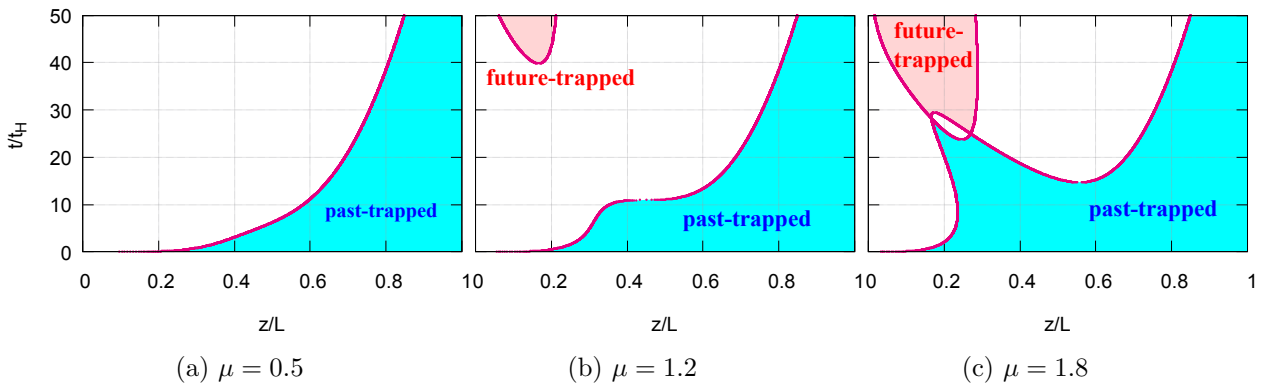


Figure 6. Configurations of the trapping horizons $R(t, r) = 2M(t, r)$. It corresponds to the points (t, r) of the compactness $2M/R = 1$ in Fig. 5.

3.3 Spacetime structures of type A/B PBH

Let us introduce the classification of trapping horizons following Refs. [42, 43]. For this purpose, to avoid confusion, we introduce another notation for the two radial null vector fields and associated expansions as l_{\pm} and θ_{\pm} for a specific trapping horizon. Then we always set $\theta_{+} = 0$ when considering a trapping horizon satisfying $\theta_{+}\theta_{-} = 0$. The classification of the trapping horizons can be summarized in Table 1.

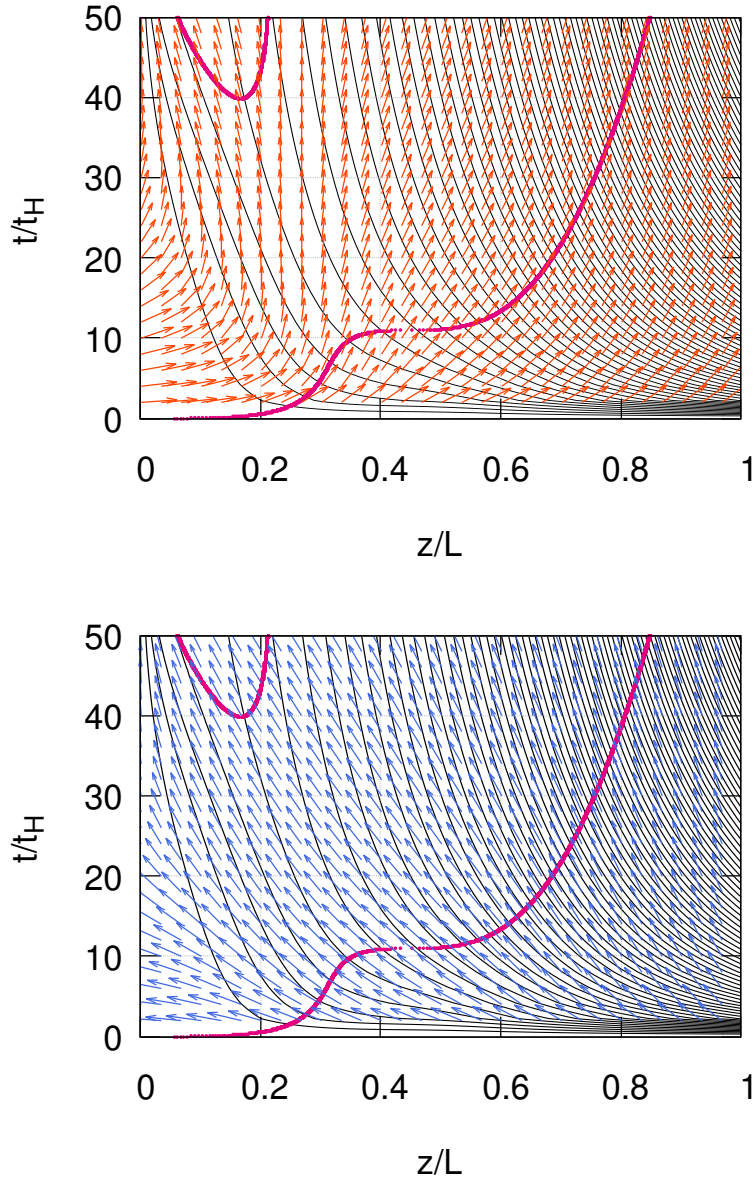


Figure 7. Directions of two independent null vector fields l and l' are depicted as orange and blue arrows for $\mu = 1.2$ case (type I) in the middle panel of Fig. 6. The R contour is plotted as black curves with 1.0 increments starting from $R = 1.0$ and increasing from left bottom to right top.

$\theta_+ = 0$	+	0	-
θ_-	Past	Bifurcating	Future
$\mathcal{L}_-\theta_+$	Inner	Degenerate	Outer

Table 1. Classification of trapping horizons satisfying $\theta_+\theta_- = 0$ [42]. A black hole, a white hole, and cosmological trapping horizons with $w = 1/3$ ($w = 0$) are identified with future-outer, past-outer, and past-degenerate (past-inner) trapping horizons, respectively.

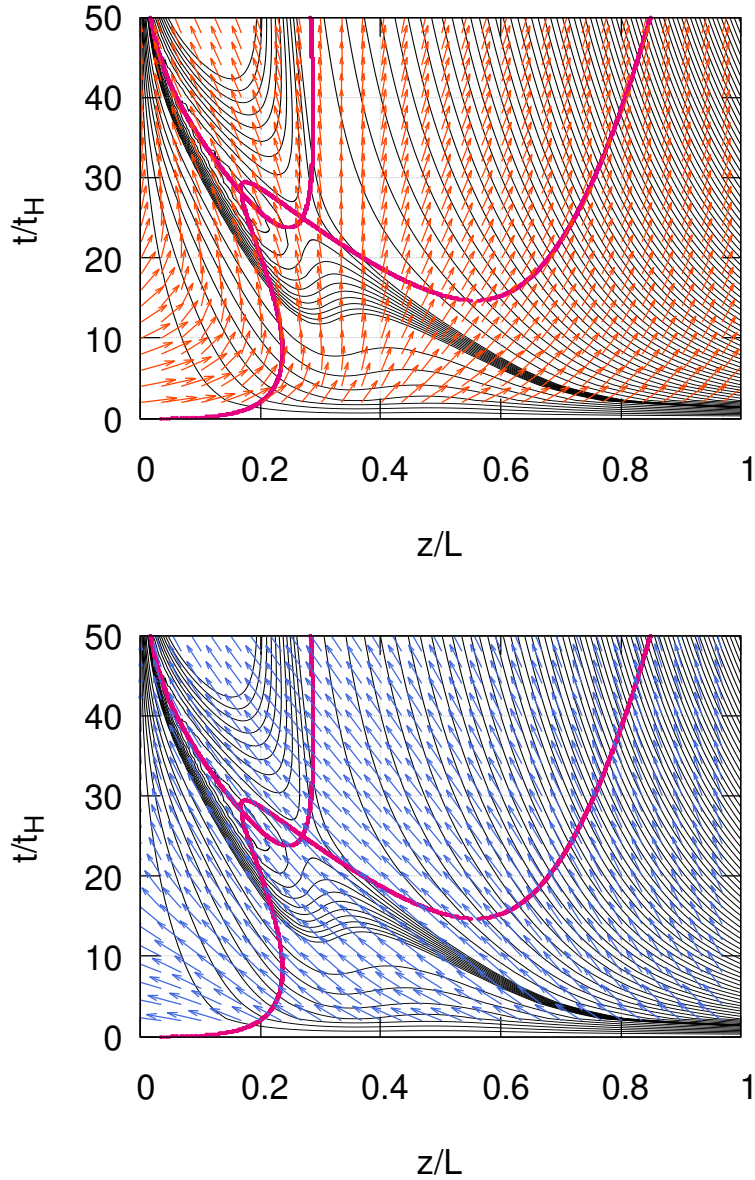


Figure 8. Directions of two independent null vector fields l and l' are depicted as orange and blue arrows for $\mu = 1.8$ case (type II) in the right panel of Fig. 6. The R contour is plotted as black curves with 1.0 increments starting from $R = 1.0$ and increasing from left bottom to right top. In addition to the original plot of R levels with increments of 1.0, it is also plotted with increments of 0.1 from $R = 8.1$ to 8.9.

Unlike the dust case discussed in Appendix A, we can only obtain numerical solutions such as those shown in Figs. 7 and 8 for the radiation case. From these figures and carefully comparing the similarities and differences from the exact conformal diagrams of the dust solution discussed in the Appendix A, we can deduce possible conformal diagrams and proper identifications of the trapping horizons for the radiation case as shown in the left and right panels in Fig. 9 as possible conformal diagrams of type A and type B PBHs, respectively.

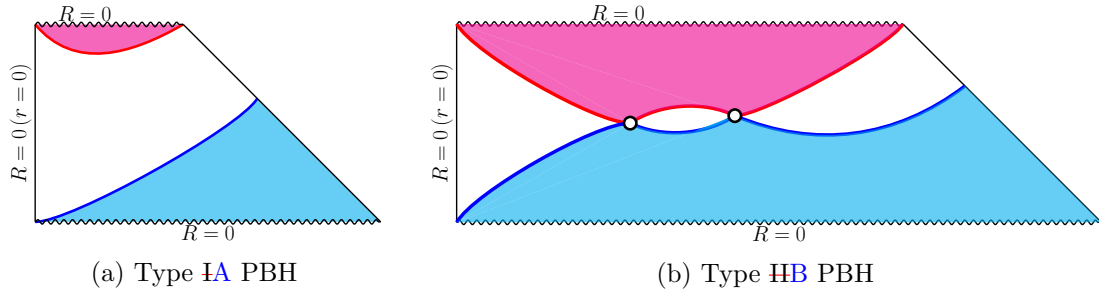


Figure 9. The present numerical results are inferred from the conformal diagrams of type A and B PBHs in radiation domination. The left figure defines a type A PBH as a causal structure of the typical case of PBH. The right one includes bifurcating trapping horizons and defines a type B PBH. The red and blue curves depict the future and past trapping horizons, respectively. The bifurcating trapping horizons ($\theta_+ = \theta_- = 0$) are depicted as circles in the type B case.

The crucial difference between the right and left panels in Fig. 9 is the existence of the bifurcating trapping horizons $(\theta_-; \mathcal{L}_-\theta_+)|_{\theta_+=0} = (0; *)$, which is described by the intersection points of the two trapping horizon trajectories in Fig. 8. In this paper, we propose to use this difference to classify the PBH formation processes into types A and B; that is, we identify the PBH as type A if there is no bifurcating trapping horizon and as type B if at least one bifurcating trapping horizon appears during the time evolution associated with the intersection point. KHW has already pointed out this difference in Ref. [1] for the case of the dust fluid. Unlike the current proposal, the authors in Ref. [1] identified the definitions of type I/II and type A/B. However, in our simulation with $w = 1/3$, we find the case of type IIA, the horizon configuration is of type A from type II fluctuation for the $\mu = 1.6$ case. This fact is our motivation for the new definition of the PBH.

The critical difference between the dust and the radiation cases is that trapping horizons in the FLRW regions are timelike and null for the former and the latter, respectively. See Figs. 15, 16 and 18 and Ref. [43]. Then, we confirm that the outermost boundary surface of the future-trapped region is the future-outer trapping horizon, which describes a BH apparent horizon. In addition, the outermost boundary surface between the past-trapped and non-trapped regions describes a cosmological apparent horizon, which asymptotically approaches the past degenerate trapping horizon in the background FLRW universe.

It is worth noting that the schematic diagram given by Fig. 9b implies that all light rays emitted from the center reach not the future null infinity but the future singularity of the type B PBH. Although we cannot make any general statement for the moment, the null trajectories indicated by the orange arrows in Fig. 8 seem consistent with this observation.

4 PBH mass

4.1 PBH mass with the Gaussian initial fluctuation

Let us introduce the mass of the PBH in two different ways at each characteristic time.⁶ The first is to calculate the Misner-Sharp mass inside the apparent horizon at its first appearance

⁶Here, we consider how the mass of the PBH depends on the initial amplitude μ of the fluctuation in the type II regime by using the three-zone model with dust as seen in Fig. 17. The mass parameter gives the PBH mass for the Schwarzschild spacetime in the middle patch. Let's fix the scale of the spatial curvature of the closed FLRW region. The horizon area of the Schwarzschild region is fixed by the horizon area on the matching surface between the closed FLRW and the Schwarzschild regions. By increasing the initial

with the future-trapped region (see Fig. 6). We refer to the mass at this time as the initial BH mass. In a type A PBH, the BH apparent horizon appears as a future-outer trapping horizon, while it appears as a bifurcating outer trapping horizon in type B. We also calculate the final PBH mass by estimating the effect of the accretion. The accretion process is well described by the mass accretion model, often called Novikov-Zeldovich or Bondi accretion [2, 44]. In this accretion model, the time evolution of the mass is given by

$$\frac{dM}{dt} = 16\pi F M^2 \rho_b, \quad (4.1)$$

where $\rho_b = \rho_{b,0}(t_0/t)^2$ is the background energy density, and F is a constant that corresponds to the efficiency of accretion, which is commonly numerically found to be of order $\mathcal{O}(1)$. It is important to note that Eq. (4.1) is not valid at the time of formation of the trapping horizon since it neglects the cosmological expansion as Carr and Hawking (1974) [4] already pointed out. However, once we have a quasi-stationary flow into the PBH, it will correctly describe the accretion into the PBHs for sufficiently long times. The integrated solution is,

$$M(t) = \frac{1}{\frac{1}{M_f} + \frac{3F}{2t}}, \quad (4.2)$$

where M_f is the final BH mass. We fix the values of M_f and F by fitting Eq. (4.2) to the numerical data in a sufficiently late finite time interval denoted in Fig. 10 together with the time evolution of the mass for each value of μ . The values of F obtained by the fitting are listed in Table 2. The value of F decreases with increasing μ , which means the accretion is getting smaller. This behavior is consistent with the results in Ref. [45].

μ	$M_f[M_{\text{H}}]$	F
1.2	11.9	5.0
1.4	14.7	5.0
1.6	16.8	4.9
1.8	18.6	4.7
2.0	20.1	4.5
2.2	21.4	4.4

Table 2. The values of F and M_f for each amplitude of μ result from the fitting in Fig. 10.

Let us check the μ dependence of the PBH mass. In Fig. 11, we plot the initial and final PBH mass values for each value of μ . The initial and final PBH masses get larger with increasing amplitude μ . We will check the dependence of the profile in the next subsection.

amplitude, we expect the closed FLRW region to be extended and the boundary to be shifted more to the right. In the closed FLRW side, the boundary shift to the right decreases the area of the horizons. Therefore, the mass parameter for the Schwarzschild region is also expected to decrease. From the above consideration of the model with dust, we may naively guess that the mass of the resultant PBH would decrease with the initial amplitude value for the type II regime. In fact, for general equations of state, the Misner-Sharp mass of the truncated closed FLRW universe is given by $4\pi\rho R^3/3$ with R being the areal radius of the outer boundary of the region, thus decreasing if the closed FLRW universe goes beyond the great sphere and approaches the “separate universe scale”, as indicated in Ref. [24]. However, as will be shown soon, this assumption is not necessarily valid for the radiation case, and the behavior also strongly depends on the profile of the initial fluctuation.

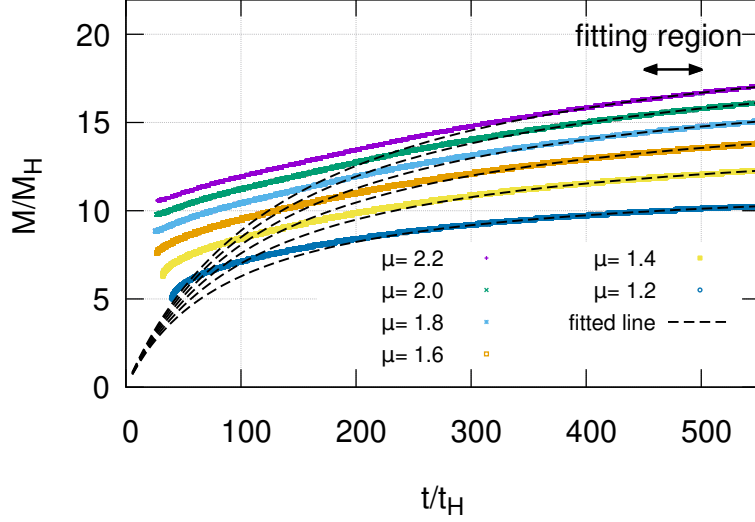


Figure 10. The time evolution of the BH mass for each value of μ . The black dashed curves are fitting curves with Eq. (4.2) including the two parameters M_f and F . The fitting region is taken for the interval between $t = 450t_H$ and $t = 500t_H$.

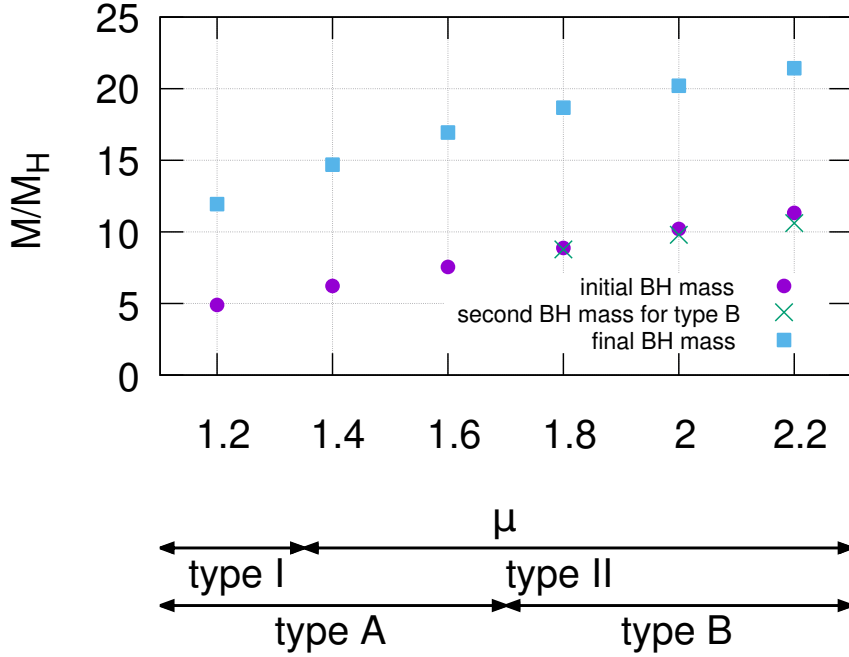


Figure 11. PBH mass in terms of the horizon mass at horizon entry M_H to the amplitude of fluctuation μ . In this case, in terms of fluctuation types, $\mu = 1.2$ is classified as type I, while $\mu = 1.4$ to 2.2 as type II, as seen in Fig. 2. In terms of formation types, on the other hand, $\mu = 1.2$ to 1.6 are classified as type A, while $\mu = 1.8$ to 2.2 as type B, as seen in Figs. 6 and 9.

4.2 PBH mass with the initial fluctuation motivated by the three-zone model

To construct a specific initial profile that can be contrasted with the former Gaussian profile, let us try to utilize the three-zone profile as a reference, an extension of the model used in Ref. [1].

Let us consider the closed FLRW region for the initial overdense region to realize a situation similar to the schematic conformal diagram. Then, as is shown in the Appendix B, under the boundary condition $\zeta = 0$ at the surface of the overdense region, we obtain the following form of $\zeta(r)$:

$$\zeta_{\text{cFLRW}}(r) = 2 \ln \frac{\cos k\chi_a/2}{\sqrt{\cos^4 k\chi_a/2 + \frac{1}{4}k^2r^2}} \quad \text{for } r \leq r_a := \frac{1}{k} \sin(k\chi_a), \quad (4.3)$$

where k^{-1} is the comoving radius of S^3 associated with the closed FLRW and $0 < \chi_a \leq \pi/k$ describes the radial coordinate of the edge of the closed FLRW region. Although this expression is relevant for the region $r \leq r_a$, we simply extend this expression in the region $r > r_a$, and to realize the condition $\zeta(L) = 0$, we use the following specific functional form of $\zeta(r)$:

$$\zeta(r) = 2\tilde{\mu} \ln(\Psi_3(r) - \Psi_3(L))W(r), \quad (4.4)$$

$$\Psi_3(r) := e^{\zeta_{\text{cFLRW}}(r)/2} + e^{\zeta_{\text{ref}}(r)/2}, \quad (4.5)$$

where $\zeta_{\text{ref}} := 0.001e^{-\frac{1}{2}k^2r^2}$ and $\tilde{\mu} := k\chi_a/\pi$. The overall factor $\tilde{\mu}$ is multiplied for convenience to realize the background flat FLRW universe in the limit $\tilde{\mu} = 0$. The value of l is fixed as $k^{-1} = 10H_b^{-1}$ as before, and the value of χ_a is set as $\pi\tilde{\mu}/k$ for a given value of $\tilde{\mu}$.

The initial profiles of ζ , R and the compaction function \mathcal{C}_{SS} are shown in Figs. 12 and 13. The tail profile is different from the original three-zone model, but it is similar to the three-zone profile around the peak of ζ . This profile also exhibits the type II feature with the neck structure for a large amplitude ($\tilde{\mu} \gtrsim 0.85$). The behavior of the horizon configuration

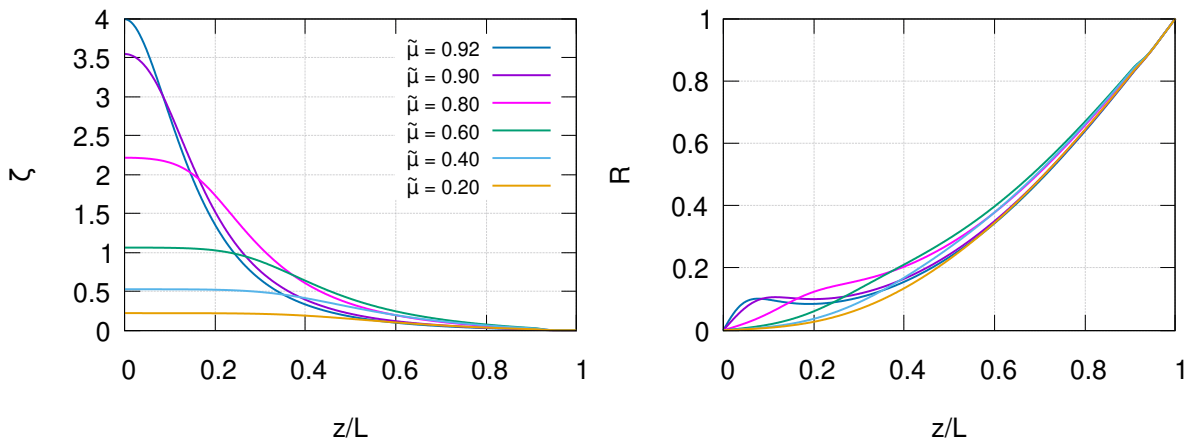


Figure 12. Initial three-zone profile of $\zeta(r)$ (left) and areal radius $R(r)$ (right) with respect to the amplitude parameter $\tilde{\mu}$. Taking the amplitude parameter $\tilde{\mu}$ larger, a type II fluctuation appeared for $\tilde{\mu}$ larger than 0.80 with the neck $\partial_r R = 0$. The original profile near the peak ζ_{cFLRW} [1] is plotted in Fig. 19 in Appendix B.

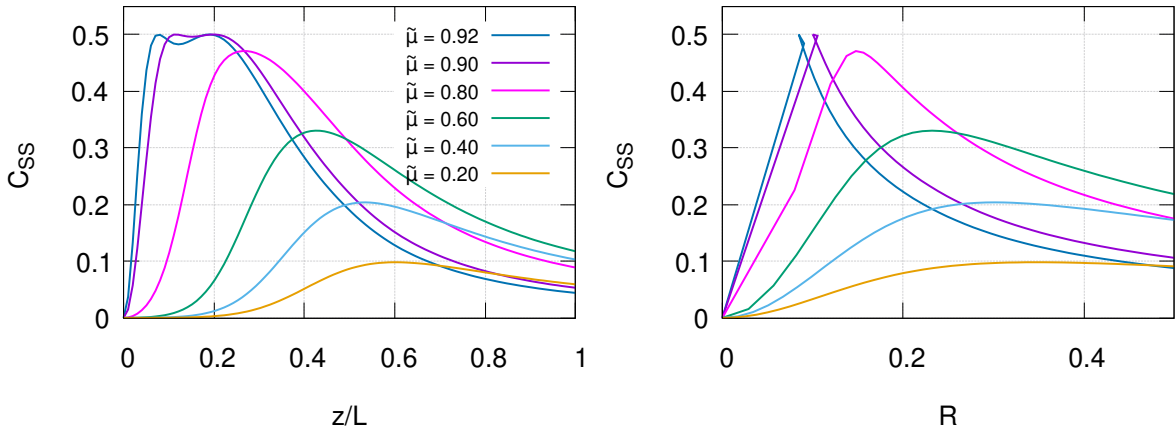


Figure 13. Compaction function $\mathcal{C}_{\text{SS}}(r)$ for thnon-linearprofile. The horizontal axis is the coordinate radius with scale-up z/L (left)/ the areal radius R (right). By taking the amplitude $\tilde{\mu}$ larger, the number of peaks becomes two for $\tilde{\mu} = 0.89$, corresponding to type II fluctuation.

is similar to the case of the Gaussian profile, and we do not explicitly show it. In contrast to the Gaussian profile, the initial PBH mass formed by this profile decreases as the amplitude of fluctuation $\tilde{\mu}$ increases for $\tilde{\mu} > 0.65$ as shown in Fig. 14, even though they are classified as type I fluctuations and formations for $\tilde{\mu} \leq 0.88$. This result, as well as the behavior of the Gaussian profile, indicates that whether the initial PBH mass increases or decreases with the amplitude parameter is not only up to its type but also strongly dependent on its profile, together with the ambiguity in quantifying the amplitude of non-linear perturbation. We also find the gap between the parameter region of type I/II and type A/B PBHs, as indicated in Fig. 14. The decreasing behavior of the initial PBH mass with the amplitude can be easily predicted by focusing on the profile of the compaction function as a function of the areal radius. The initial PBH mass would be roughly estimated by the areal radius of the peak of the compaction function at the horizon entry. Therefore, if the areal radius around the peak of the compaction function increases and decreases with the amplitude of the perturbation profile, the initial PBH mass is expected to increase and decrease, respectively. In the case of the Gaussian profile, one can find that the areal radius around the peak of the compaction function increases with the value of the amplitude μ as the right panel of Fig. 2, while it decreases with $\tilde{\mu}$ in the case of the specific profile (4.4) as the right one of Fig. 13.

5 Conclusion

We have numerically investigated the type II PBH formation from a type II initial fluctuation $\zeta(r)$, which is defined by the non-monotonicity of the areal radius $R(r) \propto r e^{\zeta}$ with respect to the coordinate radius r on the spatial geometry, i.e., the existence of $\partial_r R(r) = 0$ (called neck or throat structure), in the radiation-dominated situation. As in the dust case reported in KHW, the PBH formation process can be classified into types I and II according to the configuration of the trapped regions $R(t, r) \leq 2M(t, r)$ (or trapping horizons $R(t, r) = 2M(t, r)$). Specifically, if there is a bifurcating trapping horizon, the PBH is classified as type B, and otherwise, it is classified as type A. In the dust case, KHW reported that a type I fluctuation results in a type A PBH and a type II fluctuation in a type B PBH. However,

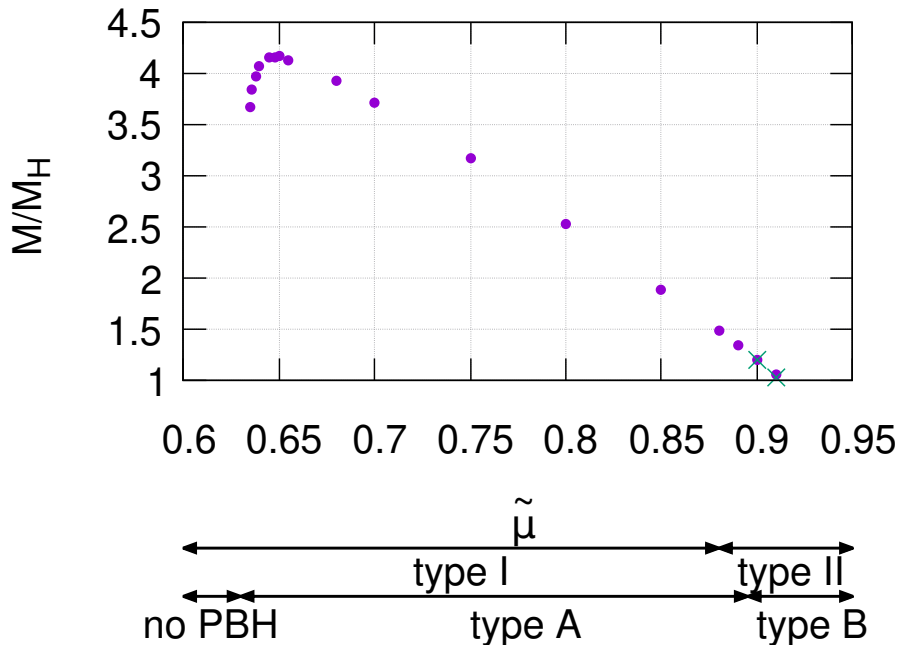


Figure 14. Initial PBH mass with respect to the amplitude of fluctuation for the three-zone profile.

in the case of radiation fluids, this is not true. We found a gap between the classifications regarding the shape of the initial spatial geometry (fluctuation type) and the structure of the trapping horizons (formation type). We found that a type II fluctuation may result in a type I PBH, so-called type II-A PBH. Therefore, we propose classifying type A/B PBHs based on the existence of the bifurcating trapping horizon independently of the type of the initial fluctuation.

In the leading order of the long-wavelength limit, the overdense region can be roughly approximated by the closed FLRW universe, and the amplitude of the density perturbation can be translated into the value of the radial coordinate at the edge of the closed FLRW region. Then, the type II fluctuation indicates that the edge is located in the other hemisphere of S^3 initial hypersurface beyond the great circle. Therefore, in the case of type II PBHs, one may expect that the PBH mass would decrease with increasing the amplitude of initial fluctuation since the initial time slice of S^3 in the overdensity region closes in the limit of large-density perturbation, which indicates that the area of the edge is vanishing. However, this is not the case for the Gaussian-type initial fluctuation profile, while the other profile exhibits decreasing mass with increasing initial amplitude. Therefore, we conclude that the behavior of the initial PBH mass depends on not only the type of fluctuation but also the fluctuation profile. Thus, a systematic investigation of the profile dependence would be needed, e.g., by using the shape parameter defined as the curvature peak of the compaction function \mathcal{C}_{SS} [19, 45]. In addition to profile dependence, dependence on the equation of state $p = w\rho$ is also an interesting issue, filling the gap between KHW and this work [20].

Acknowledgments

The authors are grateful to K.-I. Nakao, B.J. Carr, T. Igata, and J.M.M. Senovilla for

useful comments and fruitful discussion. A.E. acknowledges support from the JSPS Postdoctoral Fellowships for Research in Japan (Graduate School of Sciences, Nagoya University). The authors are supported in part by the JSPS KAKENHI Grant Nos. 19K03876(TH), 20H05850(CY), 20H05853(TH, CY), and 24KJ1223(DS). KU would like to take this opportunity to thank the “Nagoya University Interdisciplinary Frontier Fellowship” supported by Nagoya University and JST, the establishment of university fellowships towards the creation of science technology innovation, Grant Number JPMJFS2125. CY and TH acknowledge the hospitality at APCTP during the focus research program “Black Hole and Gravitational Waves: from modified theories of gravity to data analysis”, where part of this work was discussed.

A Conformal diagrams of the three-zone model for the dust case

In the three-zone model [7], the spacetime of PBH is described by the patchwork of the three different regions: the innermost overdense region is given by a spatially closed FLRW universe, the intermediate underdense region, and the outermost flat FLRW universe as the background. We also note that the intermediate underdense region must be introduced to compensate for the innermost region’s mass excess and connect the spacetime to the background spacetime without a mass gap. Without the intermediate underdense region, this model cannot be the exact solution, even for the dust case.

For the underdense region with a perfect fluid with $w = 1/3$, obtaining any analytical and exact solutions of such dynamical inhomogeneous spacetimes with non-linear sound waves would not be tractable. Therefore, we stick to the three-zone model with dust. Furthermore, for simplicity, we focus on the model where the underdense region is described by the Schwarzschild solution, where the matching is possible without any singular hypersurface for the dust case. Despite this significant simplification, the model provides a powerful tool for capturing the overall dynamics of PBH and the structure of trapping horizons. Note that one can also approach the same problem by using the Lemaître-Tolman-Bondi exact dust solution (c.f. [1]).

The conformal diagrams for the three spacetimes of which the three-zone model consists are shown in Fig. 15, where future $(\theta_-; \mathcal{L}_-\theta_+)|_{\theta_+=0} = (-; *)$, past $(+; *)$, and bifurcating $(0; *)$ trapping horizons are denoted by red lines, blue lines, and the intersection point between them in the Schwarzschild region, respectively. For the dust case $w = 0$, the apparent horizon and cosmological apparent horizon become future-outer $(-; -)$ and past-inner $(+; +)$, denoted by red-solid and blue-dashed lines, respectively.

First, let us construct the spacetime diagram of the case of the type I fluctuation. The extracted regions for the patchwork in the type I (type A) case are described by the yellow shaded regions in Fig. 15, and the resultant spacetime diagram is shown in the left panel of Fig. 17. These conformal diagrams define the right and left-directed future null vectors as l_{out} and l_{in} , respectively. For the closed FLRW region, on the boundary of the extracted region, we can find $\theta_{\text{out}} > 0$ and $\theta_{\text{in}} < 0$ at the maximum expansion. Therefore, in the outside Schwarzschild region, we also require the same sign of θ_{out} and θ_{in} . Similarly, one can understand the matching of the Schwarzschild region and the background spatially flat FLRW spacetime.

The extracted regions are yellow-shaded for the type II fluctuation in Fig. 16. Since the type II fluctuation should have a maximal value of the areal radius, the boundary of the closed FLRW region must be outside the central point at which the areal radius takes the

maximum value corresponding to the area of the big sphere at the maximum expansion. Then we find $\theta_{\text{out}} < 0$ and $\theta_{\text{in}} > 0$ on the boundary, which can be matched with the Schwarzschild region only in the left part of the Schwarzschild conformal diagram. Thus, the resultant conformal diagram for type II (type B) is given by the right panel of Fig. 17.

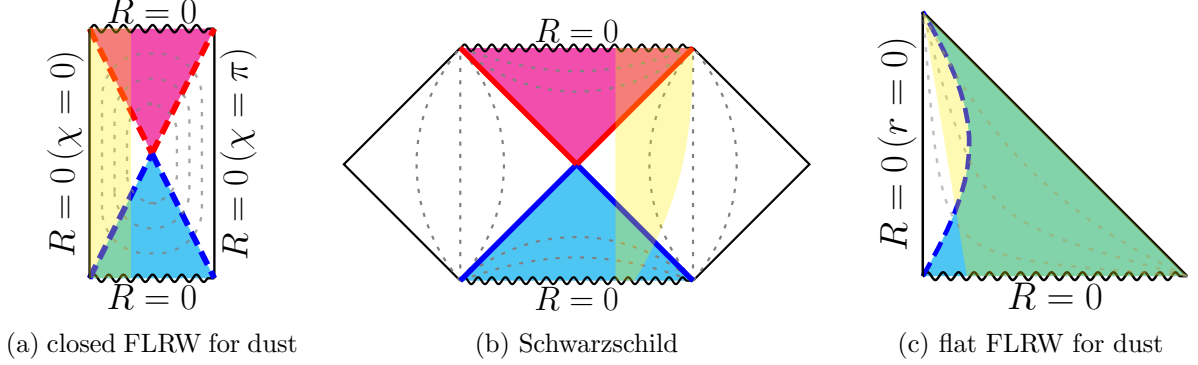


Figure 15. Conformal diagrams to use for a patchwork for the spacetime of the type I (type A) PBH schematically in Fig. 17 for dust case $w = 0$. Dashed gray curves represent R -levels. Red (blue)-shaded regions represent future (past) trapped regions. Future-outer $(\theta_-; \mathcal{L}_- \theta_+)|_{\theta_{\pm}=0} = (-; -)$, past-outer $(+; -)$, future-inner $(-; +)$, and past-inner $(+; +)$ trapping horizons are denoted by red-solid, blue-solid, red-dashed, and blue-dashed lines, respectively.

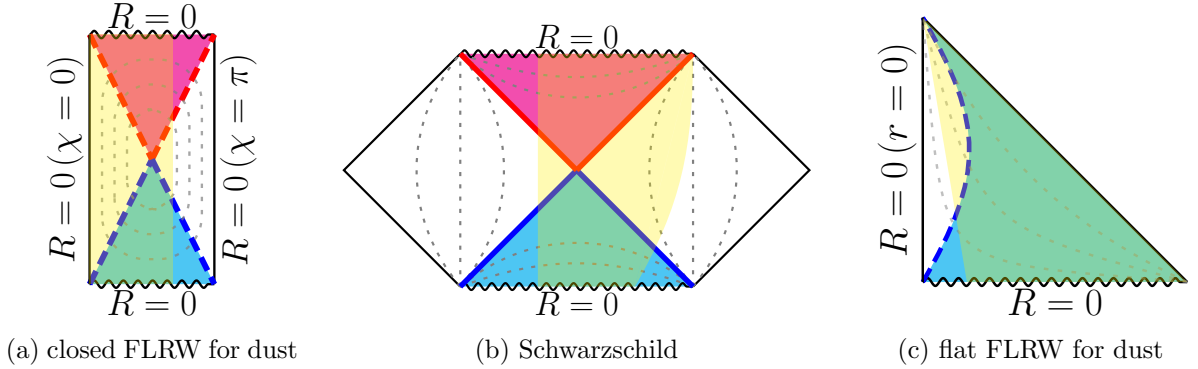


Figure 16. Same as Fig. 15 but for the type II (type B) PBH. We use the yellow-shaded regions for a patchwork.

B Derivation of ζ_{cFLRW} in radial coordinate r

The leading order of the long-wavelength solution in terms of spatial 3-metric is expressed as

$$dl^2 = a^2 e^{2\zeta(r)} (dr^2 + r^2 d\Omega^2), \quad (\text{B.1})$$

where r is a radial coordinate in the conformally flat geometry. We consider this perturbed metric of an overdense region as closed FLRW geometry with a constant positive curvature k^2 ,

$$dl^2 = a^2 \left(d\chi^2 + \frac{1}{k^2} \sin^2 k\chi d\Omega^2 \right), \quad (\text{B.2})$$

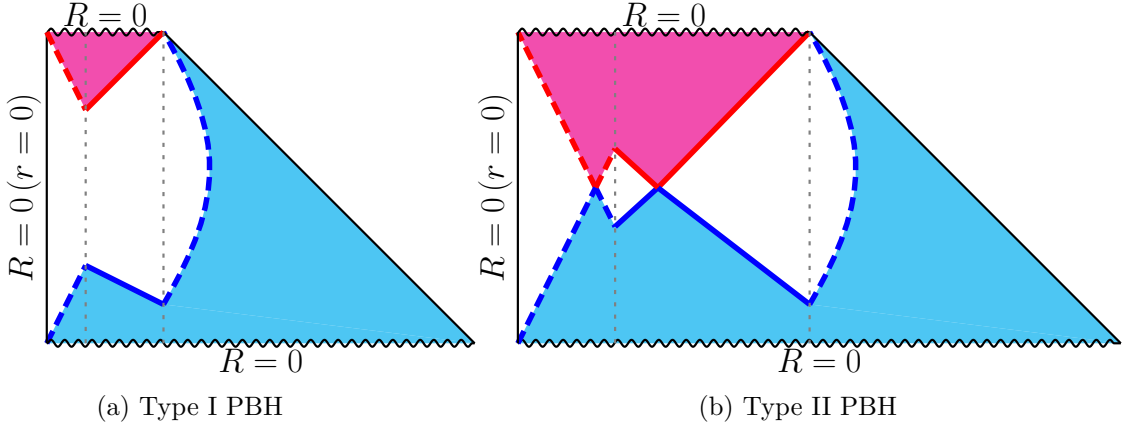


Figure 17. Conformal diagrams of PBH for dust case $w = 0$ as a patchwork of the three diagrams and trapping horizons. The left figure defines a type I (type A) PBH as a typical case PBH causal structure. The right one is constructed by changing the cutting diagram range and defining a type II (type B) PBH.



Figure 18. Conformal diagrams of the closed and flat FLRW solutions for the radiation fluid case $w = 1/3$. In this case, all trapping horizons are null. Future-degenerate $(\theta_-; \mathcal{L}_-\theta_+)|_{\theta_+=0} = (-; 0)$ and past-degenerate $(+; 0)$ trapping horizons are denoted by red-dotted and blue-dotted lines, respectively.

where χ means the comoving radial coordinate. By comparing the correspondence of the metric, we obtain

$$d\chi = \pm dre^\zeta, \quad (\text{B.3})$$

$$\frac{1}{k} \sin k\chi = re^\zeta, \quad (\text{B.4})$$

then we get the relation,

$$R = \frac{a}{k} \sin k\chi = are^\zeta, \quad (\text{B.5})$$

$$r = C \exp \int \frac{d(k\chi)}{\sin k\chi} = C \tan \frac{k\chi}{2}, \quad (\text{B.6})$$

where C is an integral constant. By using these relations, ζ is obtained as

$$e^\zeta = \frac{\sin k\chi}{kr}, \quad (\text{B.7})$$

$$= \frac{2}{Ck} \cos^2 \frac{k\chi}{2}, \quad (\text{B.8})$$

$$= \frac{2}{k} \frac{1/C}{1 + (r/C)^2}. \quad (\text{B.9})$$

If we write C as $2C'/k$ for simplicity,

$$e^\zeta = \frac{1/C'}{1 + \frac{k^2}{4}(r/C')^2} \quad \therefore \quad \zeta = \ln \frac{1/C'}{1 + \frac{k^2}{4}(r/C')^2}. \quad (\text{B.10})$$

Here we impose the boundary condition that $\zeta = 0$ for $\chi = \chi_a$, we get

$$C' = \cos^2 \frac{k\chi_a}{2}. \quad (\text{B.11})$$

Then

$$\zeta = 2 \ln \frac{\cos k\chi_a/2}{\sqrt{\cos^4 k\chi_a/2 + \frac{1}{4}k^2r^2}}. \quad (\text{B.12})$$

This functional form is shown as:

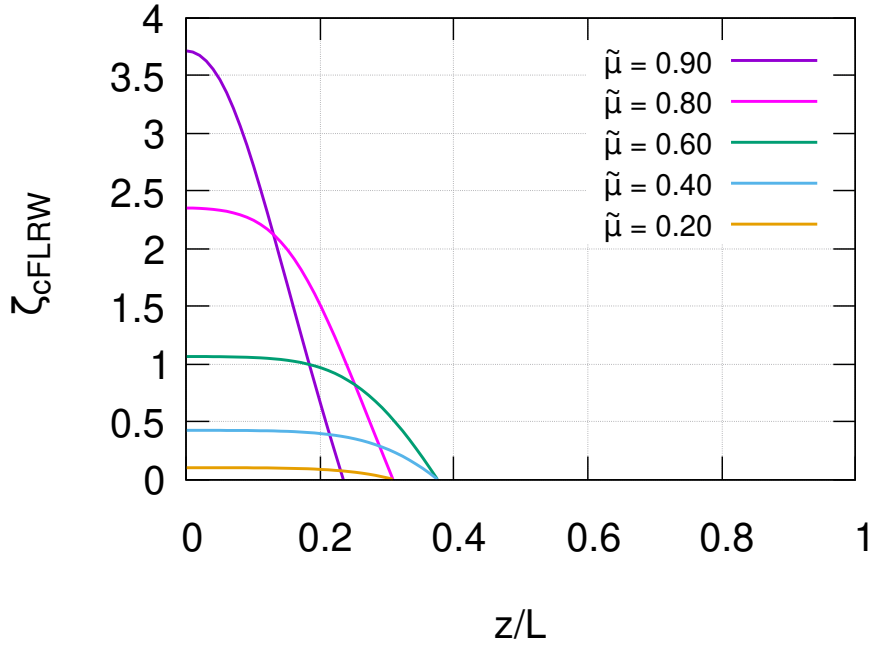


Figure 19. Functional form of ζ_{cFLRW} for overdense region $\chi \leq \chi_a$. This profile is obtained by imposing a boundary condition that $\zeta = 0$ at the edge of the overdense region $\chi = \chi_a$ [1].

C Double-peaked compaction function and averaged density perturbation in the type II fluctuation

For type II fluctuations, let us assume that $R' = \partial_r R$, where $R := ae^\zeta$ is the areal radius, satisfies the following condition

$$R' \begin{cases} > 0 & (0 < r < r_{m1}, r_{m2} < r) \\ = 0 & (r = r_{m1}, r_{m2}) \\ < 0 & (r_{m1} < r < r_{m2}) \end{cases} . \quad (\text{C.1})$$

Since

$$R' = ae^\zeta(1 + r\zeta'), \quad (\text{C.2})$$

we find $r\zeta' > -1$ for $0 < r < r_{m1}, r_{m2} < r$, $r\zeta' = -1$ for $r = r_{m1}, r_{m2}$, and $r\zeta' < -1$ for $r_{m1} < r < r_{m2}$. From the above assumption, we can deduce that $r\zeta'$ must have at least one minimum below -1 with $(r\zeta')' = 0$ between r_{m1} and r_{m2} . For simplicity, we additionally assume within this section that $r\zeta'$ takes only one minimum at $r = r_{m3}$ between r_{m1} and r_{m2} and $r\zeta'$ monotonically decreases for $0 < r < r_{m3}$ and monotonically increases for $r_{m3} < r$. Since we have the compaction function ⁷

$$C_{\text{SS}}(r) = \frac{1}{2} \left(1 - (1 + r\zeta')^2 \right) \quad (\text{C.3})$$

and its derivative

$$C'_{\text{SS}}(r) = -(1 + r\zeta')(\zeta' + r\zeta''), \quad (\text{C.4})$$

we find that the compaction function $C_{\text{SS}}(r)$ has three extrema at $r = r_{m1}, r_{m3}$ and r_{m2} with $C'_{\text{SS}}(r) = 0$, two of which at $r = r_{m1}$ and r_{m2} correspond to two peaks with the value $1/2$, and the rest at $r = r_{m3}$ to its minimum below $1/2$. This feature is typically seen for type II fluctuations and actually the case for the Gaussian-shaped profile Eq. (2.5) as seen in Fig. 20.

The density perturbation $\delta := \rho/\rho_b - 1$ in a sub-leading order $\mathcal{O}(\epsilon^2)$ of the long-wavelength solutions for uniform Hubble (constant mean curvature) slice is written as [21],

$$\delta \simeq -\frac{4}{3}e^{-5\zeta/2}\bar{\Delta}\left(e^{\zeta/2}\right)\left(\frac{1}{aH_b}\right)^2, \quad (\text{C.5})$$

where $\bar{\Delta}$ is the Laplacian of the flat background geometry. The compaction function can be identified with the volume averaged density perturbation at the horizon entry $R = 1/H_b$,

$$\bar{\delta}|_{H_b=1/R} \simeq 2C_{\text{SS}}. \quad (\text{C.6})$$

⁷One can rewrite $C_{\text{SS}}(r)$ as

$$C_{\text{SS}}(r) = -r\zeta' \left(1 + \frac{1}{2}r\zeta' \right) = \frac{3}{4}\delta_1 \left(1 - \frac{3}{8}\delta_1 \right) = -\frac{9}{32} \left(\delta_1 - \frac{4}{3} \right)^2 + \frac{1}{2},$$

where

$$\delta_1 := -\frac{4}{3}r\zeta'.$$

is the "linear-order density perturbation". Therefore, C_{SS} as a function of δ_1 takes two zeroes at $\delta_1 = 0$ and $\delta_1 = 8/3$ and a maximum $1/2$ at $\delta_1 = 4/3$. The type II fluctuation is characterized by the existence of the interval in r with $\delta_l(r) > 4/3$, where $C_{\text{SS}}(r)$ as a function of r takes two maxima $1/2$ at its boundaries with $\delta_l(r) = 4/3$.

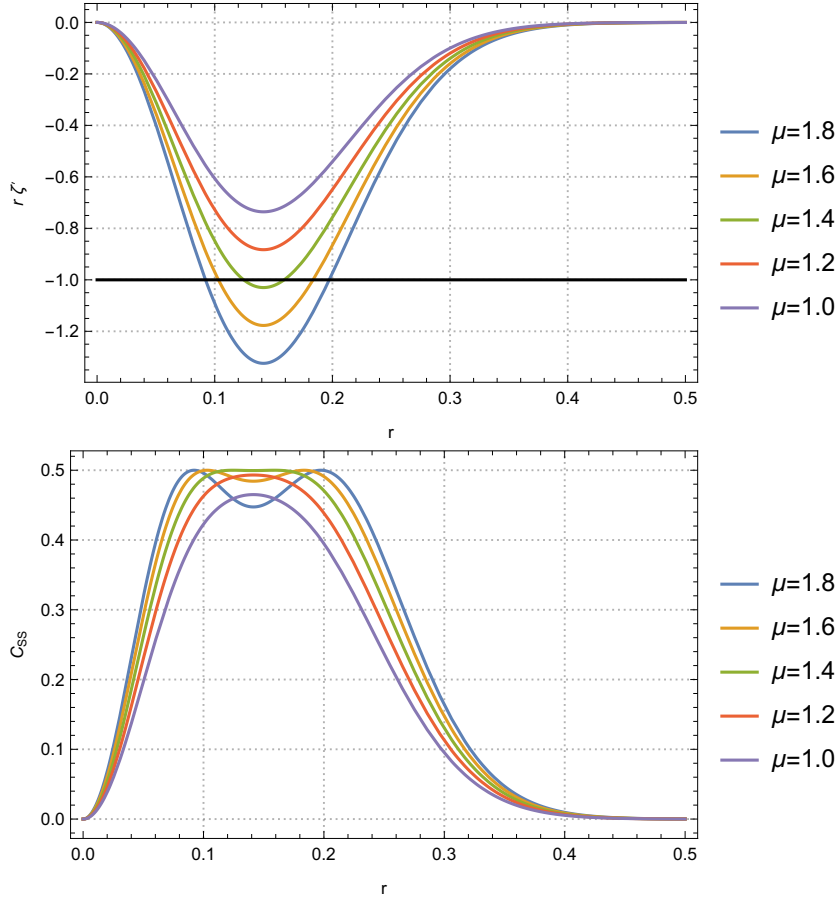


Figure 20. The situation of type II fluctuation $r\zeta' < -1$ from non-monotonicity of the areal radius R , $R' < 0$, and corresponding to the two peaks of the compaction function C_{SS} (or averaged density perturbation $\bar{\delta}$ at the horizon entry).

Then, the plot of C_{SS} in Fig. 20 can also be understood as $\bar{\delta}$ up to the factor of 2. For the type II fluctuations ($\mu \gtrsim 1.4$), the value of $\bar{\delta}$ takes a minimal value at $r = \sqrt{2}/k \simeq 0.14$ with $k = 10$, and the minimal value decreases with increasing μ .

It is worth noting that the separate universe (pinch-off) limit will not occur for this Gaussian-shaped profile of ζ , while Kopp et al. considered the limit based on the other profile via the closed FLRW (or Three-zone) geometry of Eq. (4.3) (or Eq.(4.4)).

References

- [1] M. Kopp, S. Hofmann and J. Weller, *Separate universes do not constrain primordial black hole formation*, *Phys. Rev. D* **83** (2011) 124025.
- [2] Y.B. Zel'dovich and I.D. Novikov, *The Hypothesis of Cores Retarded during Expansion and the Hot Cosmological Model*, *Soviet Astron. AJ (Engl. Transl.)*, **10** (1967) 602.
- [3] S. Hawking, *Gravitationally Collapsed Objects of Very Low Mass*, *Monthly Notices of the Royal Astronomical Society* **152** (1971) 75
[\[https://academic.oup.com/mnras/article-pdf/152/1/75/9360899/mnras152-0075.pdf\]](https://academic.oup.com/mnras/article-pdf/152/1/75/9360899/mnras152-0075.pdf).

- [4] B.J. Carr and S.W. Hawking, *Black Holes in the Early Universe*, *Monthly Notices of the Royal Astronomical Society* **168** (1974) 399 [<https://academic.oup.com/mnras/article-pdf/168/2/399/8079885/mnras168-0399.pdf>].
- [5] D.K. Nadezhin, I.D. Novikov and A.G. Polnarev, *The hydrodynamics of primordial black hole formation*, *Soviet Ast.* **22** (1978) 129.
- [6] I.D. Novikov and A.G. Polnarev, *The hydrodynamics of primordial black hole formation - Dependence on the equation of state*, *AZh* **57** (1980) 250.
- [7] T. Harada, C.-M. Yoo and K. Kohri, *Threshold of primordial black hole formation*, *Phys. Rev. D* **88** (2013) 084051.
- [8] C.-M. Yoo, *The basics of primordial black hole formation and abundance estimation*, *Galaxies* **10** (2022) .
- [9] B.J. Carr, *The primordial black hole mass spectrum*, *Astrophys. J.*, v. 201, no. 1, pp. 1-19 (1975) .
- [10] J.C. Niemeyer and K. Jedamzik, *Dynamics of primordial black hole formation*, *Phys. Rev. D* **59** (1999) 124013.
- [11] M. Shibata and M. Sasaki, *Black hole formation in the friedmann universe: Formulation and computation in numerical relativity*, *Phys. Rev. D* **60** (1999) 084002.
- [12] I. Musco, J.C. Miller and L. Rezzolla, *Computations of primordial black-hole formation*, *Classical and Quantum Gravity* **22** (2005) 1405.
- [13] T. Nakama, T. Harada, A. Polnarev and J. Yokoyama, *Identifying the most crucial parameters of the initial curvature profile for primordial black hole formation*, *Journal of Cosmology and Astroparticle Physics* **2014** (2014) 037.
- [14] T. Nakama, *The double formation of primordial black holes*, *Journal of Cosmology and Astroparticle Physics* **2014** (2014) 040.
- [15] B.J. Carr, *The primordial black hole mass spectrum.*, *ApJ* **201** (1975) 1.
- [16] A.G. Polnarev and I. Musco, *Curvature profiles as initial conditions for primordial black hole formation*, *Classical and Quantum Gravity* **24** (2007) 1405.
- [17] I. Musco, J.C. Miller and A.G. Polnarev, *Primordial black hole formation in the radiative era: Investigation of the critical nature of the collapse*, *Class. Quant. Grav.* **26** (2009) 235001 [[0811.1452](https://arxiv.org/abs/0811.1452)].
- [18] I. Musco and J.C. Miller, *Primordial black hole formation in the early universe: critical behaviour and self-similarity*, *Classical and Quantum Gravity* **30** (2013) 145009.
- [19] A. Escrivà, C. Germani and R.K. Sheth, *Universal threshold for primordial black hole formation*, *Phys. Rev. D* **101** (2020) 044022 [[1907.13311](https://arxiv.org/abs/1907.13311)].
- [20] A. Escrivà, C. Germani and R.K. Sheth, *Analytical thresholds for black hole formation in general cosmological backgrounds*, *Journal of Cosmology and Astroparticle Physics* **2021** (2021) 030.
- [21] T. Harada, C.-M. Yoo, T. Nakama and Y. Koga, *Cosmological long-wavelength solutions and primordial black hole formation*, *Phys. Rev. D* **91** (2015) 084057.
- [22] I. Musco, *Threshold for primordial black holes: Dependence on the shape of the cosmological perturbations*, *Phys. Rev. D* **100** (2019) 123524 [[1809.02127](https://arxiv.org/abs/1809.02127)].
- [23] I. Musco, V. De Luca, G. Franciolini and A. Riotto, *Threshold for primordial black holes. II. A simple analytic prescription*, *Phys. Rev. D* **103** (2021) 063538 [[2011.03014](https://arxiv.org/abs/2011.03014)].
- [24] B.J. Carr and T. Harada, *Separate universe problem: 40 years on*, *Phys. Rev. D* **91** (2015) 084048.

- [25] A.D. Gow, H. Assadullahi, J.H.P. Jackson, K. Koyama, V. Vennin and D. Wands, *Non-perturbative non-Gaussianity and primordial black holes*, *EPL* **142** (2023) 49001 [2211.08348].
- [26] A. Escrivà, V. Atal and J. Garriga, *Formation of trapped vacuum bubbles during inflation, and consequences for PBH scenarios*, *JCAP* **10** (2023) 035 [2306.09990].
- [27] H. Deng and A. Vilenkin, *Primordial black hole formation by vacuum bubbles*, *Journal of Cosmology and Astroparticle Physics* **2017** (2017) 044.
- [28] H. Deng, J. Garriga and A. Vilenkin, *Primordial black hole and wormhole formation by domain walls*, *Journal of Cosmology and Astroparticle Physics* **2017** (2017) 050.
- [29] C.W. Misner and D.H. Sharp, *Relativistic equations for adiabatic, spherically symmetric gravitational collapse*, *Phys. Rev.* **136** (1964) B571.
- [30] P.D. Lasky and A.W.C. Lun, *Generalized lemaître-tolman-bondi solutions with pressure*, *Phys. Rev. D* **74** (2006) 084013.
- [31] C.-M. Yoo, T. Ikeda and H. Okawa, *Gravitational collapse of a massless scalar field in a periodic box*, *Classical and Quantum Gravity* **36** (2019) 075004.
- [32] M. Shibata and T. Nakamura, *Evolution of three-dimensional gravitational waves: Harmonic slicing case*, *Physical Review D* **52** (1995) 5428.
- [33] T.W. Baumgarte and S.L. Shapiro, *Numerical integration of einstein's field equations*, *Phys. Rev. D* **59** (1998) 024007.
- [34] M. ALCUBIERRE, B. BRÜGMANN, D. HOLZ, R. TAKAHASHI, S. BRANDT, E. SEIDEL et al., *Symmetry without symmetry: Numerical simulation of axisymmetric systems using cartesian grids*, *International Journal of Modern Physics D* **10** (2001) 273 [<https://doi.org/10.1142/S0218271801000834>].
- [35] D.H. Lyth, K.A. Malik and M. Sasaki, *A general proof of the conservation of the curvature perturbation*, *Journal of Cosmology and Astroparticle Physics* **2005** (2005) 004.
- [36] T. Harada, C.-M. Yoo and Y. Koga, *Revisiting compaction functions for primordial black hole formation*, *Phys. Rev. D* **108** (2023) 043515 [2304.13284].
- [37] A. Escrivà and C.-M. Yoo, *Primordial Black Hole formation from overlapping cosmological fluctuations*, **2310.16482**.
- [38] C.-M. Yoo, H. Okawa and K.-i. Nakao, *Black-hole universe: Time evolution*, *Phys. Rev. Lett.* **111** (2013) 161102.
- [39] H. Okawa, H. Witek and V. Cardoso, *Black holes and fundamental fields in numerical relativity: Initial data construction and evolution of bound states*, *Phys. Rev. D* **89** (2014) 104032.
- [40] C.-M. Yoo, T. Harada, S. Hirano, H. Okawa and M. Sasaki, *Primordial black hole formation from massless scalar isocurvature*, *Phys. Rev. D* **105** (2022) 103538.
- [41] S.A. Hayward, *Gravitational energy in spherical symmetry*, *Phys. Rev. D* **53** (1996) 1938 [gr-qc/9408002].
- [42] S.A. Hayward, *General laws of black hole dynamics*, *Phys. Rev. D* **49** (1994) 6467.
- [43] T. Harada, B.J. Carr and T. Igata, *Complete conformal classification of the friedmann–lemaître–robertson–walker solutions with a linear equation of state*, *Classical and Quantum Gravity* **35** (2018) 105011.
- [44] H. Bondi, *On spherically symmetrical accretion*, *MNRAS* **112** (1952) 195.
- [45] A. Escrivà and A.E. Romano, *Effects of the shape of curvature peaks on the size of primordial black holes*, *Journal of Cosmology and Astroparticle Physics* **2021** (2021) 066.